Formation of Nickel Dendritic Crystals with Peculiar Orientations by Magnetic-Induced Aggregation and Limited Diffusion

Jing Ye, Qian-Wang Chen,* Hai-Ping Qi, and Nan Tao

Hefei National Laboratory for Physical Sciences at Microscale and Department of Materials Science & Engineering, University of Science and Technology of China, Hefei, Anhui, 230026, P. R. China

ABSTRACT: Micrometer scaled nickel dendritic crystals with distinctive style were synthesized via a self-assembled solution route without any surfactant. Structure characterizations suggest that the dendritic crystal shows first preferential orientation along [111] which is the magnetic easy axis of cubic nickel crystal and subsequently along [100], which differs from the prevalent dendritic fractals synthesized in nonequilibrium system. A formation process is proposed to illustrate the growth of ferromagnetic nickel microleaves. Additionally, the magnetic properties of nickel microleaf have been observed, which demonstrates that the saturation magnetization (Ms) and the coercivity (Hc) are 48 emu/cm^{-3} and 77 Oe, respectively. The relatively high Ms and low Hc for as-prepared product could be attributed to its special structure.

1. Introduction

In the realm of crystal growth, considerable attention has been focused on dendritic fractals, which show distinct size, shape, and chemical behavior and thus provide much promise for design and fabrication of materials with advanced functionalities.[1–7] In the prior research, a variety of dendritic crystals such as metal,[8,9] metal oxide,[10,11] and chalcogenide[12] with dendrite-like morphology have been extensively studied theoretically and experimentally. Several models including diffusion limited aggregation (DLA)[13,14] and cluster−cluster aggregation (CCA)[15,16] have been widely used to explain and analyze the formation of dendritic crystals in nonequilibrium systems. Generally, single-crystalline dendritic fractals have crystallographically equivalent growth direction, usually [100] for cubic phase and [1$\bar{1}$00] for hexagonal phase. For example, the formation of cubic galena dendrite can be regarded as preferential symmetric growth along the crystallographically equivalent [100] direction,[17] while the formation of hexagonal dendritic hematite is condidered as symmetric growth along its six crystallographically equivalent directions [1$\bar{1}$00].[18] Dendritic patterns in low-symmetry materials have also been observed.[19] The DLA and CCA methods are apparently not suitable for dealing with the crystals without unique orientations. What if more than one orientation direction is involved in the growth of dendritic fractals? Since few reports have concentrated on this situation, particularly on the magnetic dendritic materials, it is desirable to explore efficient methods to achieve the dendritic fractals with peculiar orientations and novel geometrical morphologies.

Nanoscale magnetic materials have attracted intensive interest because of their physical properties and potential technological application.[20–22] The magnetic properties of nanomaterials have been considered to be highly dependent on their size, structure, cryastallinity etc. For example, Zhu et al. have reported that the magnetic behavior of Mn_3O_4 nanocrystals was sensitive to crystal size.[23] Liu et al. have revealed that the remarkably enhanced magnetic properties of nickel nanobelts may be attributed to their beltlike structure and very small thickness.[24] Moreover, Xiong et al. have reported that the high saturation magnetization indicated the high crystallinity of the as-prepared

magnetite nanocubes.[25] Based on these reports, it is desirable to study the relationship between the magnetic properties of nanomatetials and their structure and morphology.

Herein, we offer the first opportunity to prepare single-crystalline cubic nickel dendritic fractal. The microleaves were synthesized by reduction of nickel ions in a surfactant-free aqueous environment with the existence of sodium hypophosphite as reducing agent. The as-synthesized nickel dendrites show first preferential orientation along [111] and subsequently along [100], which differs from the reported magnetic dendrites with unique single orientations.[26,27] The formation process in this system has been investigated according to the designed experiment. Meanwhile, combined with its peculiar structure, the magnetic properties of the sample, which shows relatively high saturation magnetization and low coercivity compared with other nickel nanomaterials,[28–30] are discussed.

2. Experimental Section

Preparation. All the reagents purchased from Shanghai Reagent Co. of Chinese Medical were of analytical grade and used without further purification. In a typical procedure, nickel dichloride ($NiCl_2 \cdot 6H_2O$, 0.25 mmol) and sodium hypophosphite ($NaH_2PO_2 \cdot H_2O$, 2.0 mmol) were dissolved in 50 mL of distilled water. Then ammonia hydrate (2 mL, 25% mass ratio) was added. Finally, the precursor solution was transferred into a Teflon-lined stainless-steel autoclave with the capacity of 50 mL. The autoclave was maintained at 160 °C for 24 h and then cooled to room temperature naturally. The black products were collected by applying a cylindrical self-made permanent NdFeB magnet (∼0.20 T, ∅ 50 mm × 12 mm), and the supernatant was discarded by decantation. The as-prepared black precipitate was washed with distilled water and ethanol several times and finally dried in air at 50 °C for 6 h.

Characterization. The phase and purity of the product was determined by powder X-ray diffraction (XRD) analyses (Philips X'Pert Pro Super diffract meter with Cu Kα radiation, λ = 1.54178 Å). The high-resolution X-ray photoelectron spectrum (XPS) was obtained on a VG ESCALAB MKII electron spectrometer with the X-ray source of Mg Kα. Field emission scanning electron microscopy (FESEM) images were carried out on a JEOL JSM-6700 M scanning electron microscope. Transmission electron microscopy (TEM) images were taken on a Hitachi model H-800 instrument with a tungsten filament, using an accelerating voltage of 200 kV. High-resolution transmission electron microscopy (HRTEM) images and selected area electron diffraction (SAED) patterns were recorded with a JEOL-2010 transmission electron microscope operating at 200 kV. A superconducting quantum interference device (SQUID, Quantum Design MPMS)

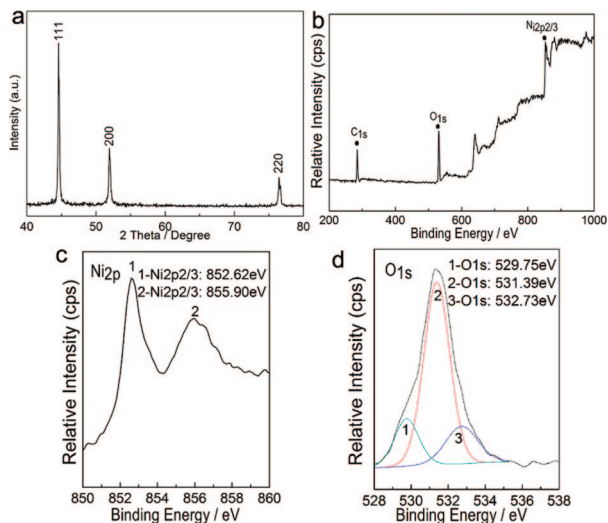* Corresponding author. Phone: +86-551-3607292. Fax: +86-551-3607292. E-mail:cqw@ustc.edu.cn.

Figure 1. (a) XRD pattern of dendritic microleaf cystallites prepared at 160 °C for 24 h; (b) XPS spectra of as-prepared sample; (c) Ni_{2p} XPS spectrum; (d) O_{1s} XPS spectrum.

magnetometer was used to measure the magnetic properties of the products. The hysteresis loops of the sample were recorded at 300 K in a magnetic field applied varying from −10000 to +10000 Oe.

3. Results and Discussion

A typical XRD pattern of the as-prepared black powder is shown in Figure 1. All of the peaks can be indexed as face-centered cubic (fcc) Ni with lattice constant of $\alpha = 3.523$ Å, which is consistent with the value given in the standard card (JCPDS 04-0850). The peaks are sharp, suggesting the good crystallinity of as-prepared product. According to Scherrer's equation $(D = K\lambda/(\beta \cos \theta))$ from the full width at half-maximum (fwhm) of (111), we have calculated that the average crystallite size in the dendritic particles is about 82 nm, which is far larger than the critical size of single magnetic domains of nickel crystal (21.2 nm).[31] No other peaks of impurities, such as nickel oxide or nickel hydroxide, could be detected, which implies that phase-pure cubic nickel can be obtained under the current synthesis conditions. To figure out the components of surface of nickel dendrites, XPS analysis was conducted. Figure 1b shows the survey XPS spectrum of the as-synthesized nickel dendrites. The binding energies obtained in the XPS analysis were corrected for specimen charging by referencing the C_{1s} line to 284.60 eV. The O_{1s} signal arises from the nickel oxides on the surface maybe because the sample is exposed to air before characterization. Figures 1c and 1d show the high-resolution XPS spectra of Ni_{2p} and O_{1s} region. The binding energy of 852.62 eV can be assigned to nickel atoms[32] in the species while the binding energy of 855.90 eV can be assigned to Ni^{2+} in the surface nickel oxide (Figure 1c).[33] There are three oxygen contributions existing in the species (Figure 1d). The binding energy of 529.75, 531.39 and 532.73 eV can be severally assigned to oxygen element in Ni−O, adsorbed oxygen molecules and O−H.[33–35] Based on the results of XPS, it can be conjectured that parts of the surface of nickel dendrites were oxidized to nickel oxide, which cannot be detected by XRD analysis due to their quite low percentage composition.

Figures 2a−c show the typical FESEM images of nickel microleaves obtained with concentration of $NiCl_2$ of 0.25 mmol (sample 1) at 160 °C for 24 h. The low magnification FESEM image (Figure 2a) indicates that the product consists of a majority of such dendritic structures revealing the high yield
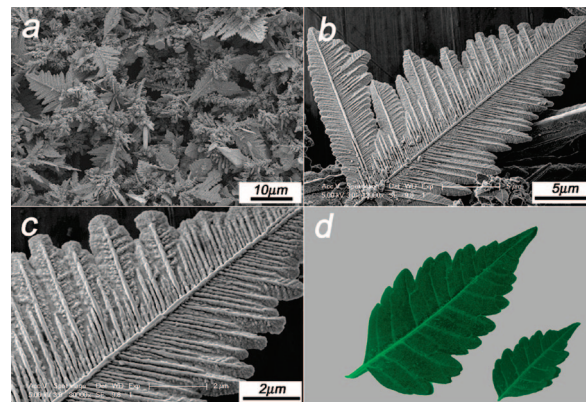

Figure 2. (a) A typical low-magnification FESEM image showing the high yield and good uniformity; (b) FESEM image of a single Ni dendritic microleaf; (c) a high magnification image of a single Ni dendritic microleaf in (b); (d) illustration of leaves.
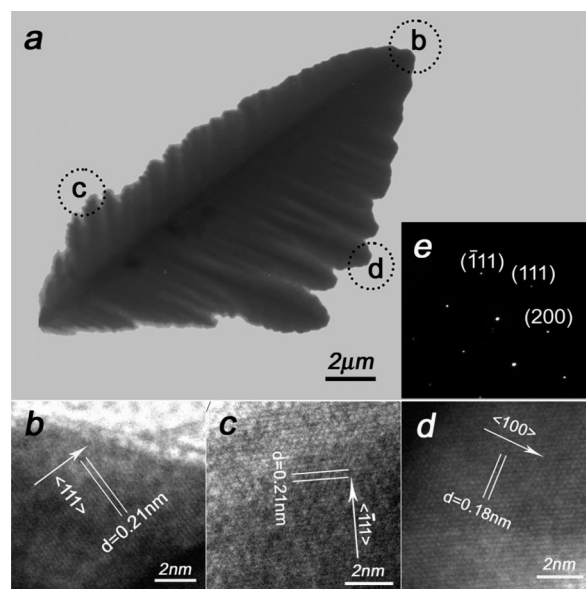

Figure 3. (a) TEM image of a single dendritic microleaf. (b−d) High-resolution TEM images recorded in different part labeled by the dashed black circle in (a) indicating the well-defined single-crystalline nature. (e) Electron diffraction pattern recorded from the entire dendritic structure also shows the single-crystalline of Ni dendritic microleaf.

and favorable uniformity achieved through this approach. The average length of leaves is about 20 μm. The front image of a single microleaf shown in Figure 2b indicates that the nearer the peak of the stem, the shorter the branch is. High-magnification images of a single leaf are presented in Figure 2c, which reveal a clear and dendritic fractal structure with a pronounced trunk consisting of corrugations and highly ordered branches distributed on both sides of the stem. Notably, the angles between the stem and bilateral branches are actually not equally: one is ca. 55° while another is ca. 70°. Figure 2d presents a photo of leaves, which appears much like the as-synthesized product.

Figure 3a shows a TEM image of an individual microleaf which exhibits distinct dendritic microleaf structures. Further structural characterization was carried out by HRTEM. Figures 3b−d show the HRTEM images taken from the areas labeled b−d (the dashed black circle part in Figure 3a), which severally show the lattice structures at the tip of the stem, the tip of the left branch, and the tip of the right branch. They all show clear
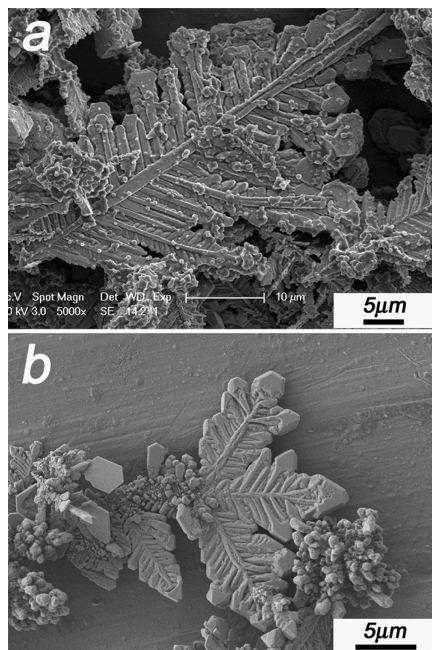
Figure 4. FESEM images of nickel dendrites obtained at reaction temperatures of 180 and 200 °C while keeping the other experimental conditions the same.

lattice fringes that indicate single crystal of the entire dendritic microleaf structure. The lattice spacing of 2.1 Å in Figures 3b and 3c corresponds to the distance of adjacent {111} facets, whereas the lattice spacing of 1.8 Å in Figure 3d corresponds to the distance of adjacent {200} facets. The selected-area electron diffraction (SAED) pattern shown in Figure 3e taken from the entire dendrite clearly confirms the microleaf to be single-crystalline. It can be indexed as the (111), ($\bar{1}$11) and (200) planes of fcc Ni. The HRTEM images associated with the SAED pattern indicate that the leaf stem is oriented along [111] and the bilateral branches are severally oriented along [$\bar{1}$11] and [100]. Therefore, the structure of the microleaf can be regarded as a first preferential growth along [111] (the stem and the unilateral branch) and subsequent growth along [100] (the other unilateral branch).

The reaction temperature and the concentration of $NiCl_2$ and reductive NaH_2PO_2 are crucial parameters to the formation of the microleaf. In our control experiments, when the temperature was raised from 160 to 180 °C and finally to 200 °C while keeping the other reaction conditions unchanged, an obvious morphology evolution from thin to thick microrod-branched dendrites was observed (Figure 4a,b). With the increasing of the reaction temperature, the branches of the microleaves became thicker, and more particles appeared. However, if the temperature was lower than 160 °C, 140 °C for example, the reaction could not be carried out. The concentration of $NiCl_2$ and reducing agent also seriously affected the generation of dendritic microleaf morphology. TEM images of samples prepared with concentration of $NiCl_2$ of 0.125 and 0.50 mmol while maintaining the ratio of $NiCl_2/NaH_2PO_2$ unchanged are presented in Figure 5a,b. The morphology of the sample with decreased $NiCl_2$ is similar to that of sample 1. However, when increasing the concentration of $NiCl_2$, distinct dendritic structures disappeared. There are many particles aggregating like a pine tree. When the concentration of reducing agent was decreased to 1.0 mmol, combined with the black product TEM image of which indicates the relative indistinct dendritic microleaf structure (Figure 5c), there is a little green powder which can be indexed
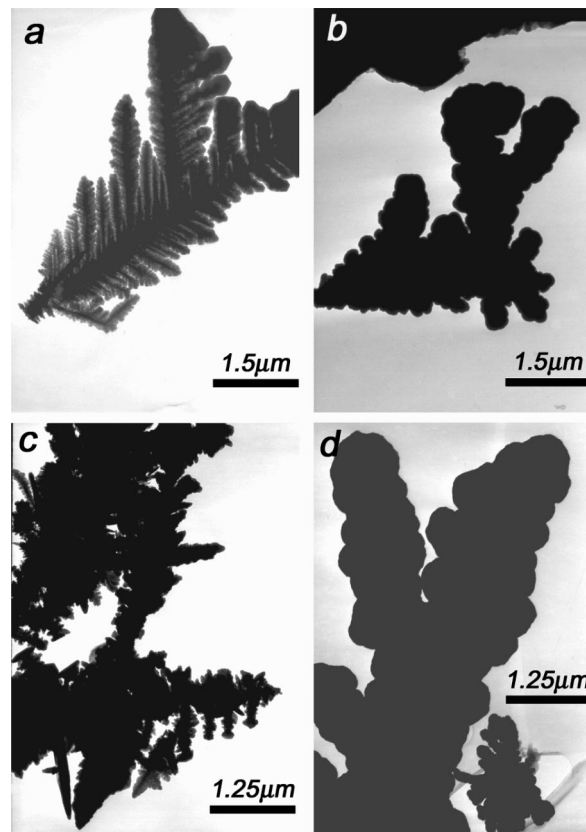

Figure 5. (a, b) TEM images of nickel dendrites prepared with the concentration of $NiCl_2$ of 0.125 and 0.50 mmol while maintaining the ratio of $NiCl_2/NaH_2PO_2$ unchanged. (c, d) TEM images of Ni dendrites obtained with the concentration of $NiCl_2$ of 0.25 mmol and the concentration of reducing agent of 1.0 and 3.0 mmol, respectively.

as pure $Ni(OH)_2$ (JCPDS 14-0117) (Figure S1 in Supporting Information). Thick rock-branched dendrites with an unclear dendritic fractal structure were observed (Figure 5d), while increasing the concentration of reducing agent from 2.0 to 3.0 mmol. On the basis of the results above, it can be concluded that high reaction temperature and concentration of $NiCl_2$ and reducing agent have a bad effect on the formation of distinct structure of dendritic microleaf. Therefore, it is possible to control the morphology of the dendritic structures simply by controlling the reaction parameters, such as reaction temperature and concentration of reactants.

The formation of the microleaf dendrites could be explained by the model proposed in Figure 6. Generally, the evolution of $c(r,t)$, the Ni(II) ion concentration in the solution at arbitrary position r and time t, is described by the diffusion equation[36]

$$\partial c(r, t)/\partial t = -\nabla \cdot \vec{j} \qquad (1)$$

where $\vec{j}$ is the flux of Ni(II) ions.[37] In this hydrothermal system, some nickel ions were first reduced by NaH_2PO_2 to nickel nuclei. These ferromagnetic nuclei generate a magnetic field which could induce paramagnetic nickel ions (Figure 6a).[38] Because of the magnetic-field-induced-effect, the evolution of the Ni(II) ion concentration in the solution in this system can be described as follows:

$$\partial c(r, t, m)/\partial t = -k\nabla \cdot \vec{j} \qquad (2)$$

where m is the magnetic-field intensity and k is the variable parameter related to m. It is known that the magnetic anisotropy energy (MAE) is the lowest when magnetizing along the

magnetic easy axis. [111] is the magnetic easy axis of a cubic nickel crystal.[39] Accordingly, the [111] direction rather than other one initiated fast growth, and then generated a pole which was possible if the growth along [111] was much faster than along the other directions. It is known that the intensity of magnetic field in both ends of the pole magnet is stronger than other position. So a great many nickel ions preferentially aggregated at the bottom due to the strong magnetic induction effect. This can be confirmed by the phenomenon that there are some particles aggregating at the bottom of the single microleaf shown in Figure 6f. With the aggregation of nickel ions, the concentration of nickel ions at the bottom increased, resulting in the enhancement of electrode potential, which made Ni(II) ions easier to be reduced by NaH_2PO_2 to form nickel storage. Then the reduced nuclei were transported from the bottom to the tip, just like the tree imbibing nutrition from its root and transporting it from the bottom to the tip along the tree stem (Figure 6b). With the transportation of nuclei, which is limited diffusion because of the low concentration of nickel, the growth of the [$\bar{1}11$] direction begins to form one unilateral branch, and subsequent growth of [100] to form the other unilateral branch (Figure 6c). With the process of reaction, all of the branches become bigger and thicker (Figure 6d) and finally interconnected to form the dendritic microleaf structures (Figure 6e). In general, the low concentration of nickel, the magnetic field induction and the nickel transportation play important roles in the dendritic microleaf structure formation.

To verify the rationality of the model, we synthesized the metal copper under the same reaction conditions as sample 1. The typical FESEM image shown in Figure 7 indicates the spherical structure instead of dendritic microleaf. It is known that elemental copper is an antimagnetic material; there is no magnetic induction effect to attract copper ions to aggregate among the nuclei during the course of the reaction. So the nuclei deoxidized from copper ions grew all over the hydrothermal system to get the spherical structures. Besides, the proposed new model could be employed to elucidate the formation process
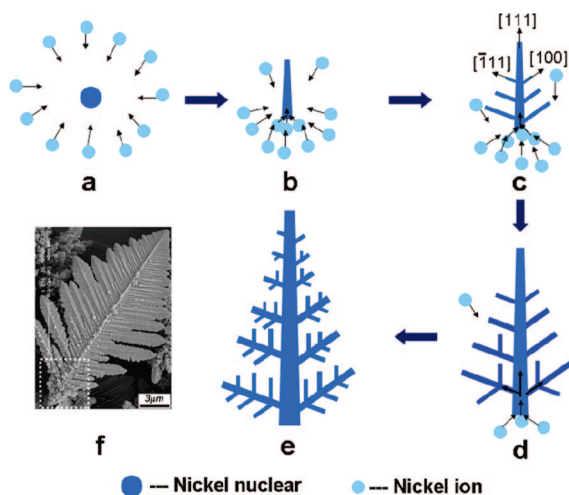

Figure 7. A typical FESEM image of copper synthesized with the same reaction conditions of nickel sample.

Figure 8. Magnetic hysteresis loop of as-prepared nickel dendritic microleaf measured at 300 K. The top left inset is an expanded low-field hysteresis curve.

of other ferromagnetic material. For instance, it has been reported that cobalt was produced with a similar dendritic structure.[26,27,40] Like nickel, a ferromagnetic cobalt nucleus can also generate a magnetic induction effect.

It is known that the magnetic properties of nanomaterials are closely related to the sample structure, crystallinity, shape anisotropy etc. The magnetic hysteresis loop (M-H loop) (Figure 8) combined with the expanded low-field hysteresis curve (inset of Figure 8) of the dendritic crystal measured at 300 K indicates the magnetic properties including saturation magnetization Ms and the coercivity Hc. Ms for the sample is 48 emu/g. Generally speaking, Ms for nanoscale magnetic materials is lower than that for corresponding bulk material because the spin disorder on the surface and surface oxidation would significantly reduce the total magnetic moment.[41] However, Ms for as-prepared product is very close to the value of bulk nickel material (Ms = 55 emu/g),[42] which may attribute to the high crystallinity of as-prepared dendritic microleaves.[43] The inset of Figure 8 shows that the Hc value for the sample is 77 Oe, which is lower than that of the bulk material (Hc = 100 Oe).[42] In addition, it is notable to see that Hc for the sample is also much lower than that of similarly sized nickel microcrystals prepared by the other approach (Hc = 215 Oe).[44] As mentioned above, the stem orientation of the dendritic microleaf is along the [111] axis, which is the magnetic easy axis of a cubic nickel crystal. Accordingly, the low magnetocrystalline anisotropy may be responsible for the quite low Hc value.[45]

Figure 6. Schematic illustration of the formation process of Ni microleaf dendrites. (a) Ferromagnetic nickel nuclear induced nickel ions. (b) Formation of a stem and meanwhile a great deal of nickel ions were induced to aggregate among the bottom, then transported from the bottom to the tip along the stem. (c and d) Growth of the stem and the branches. (e) All of the branches become bigger and thicker and finally interconnected to form the dendritic microleaf structures. (f) FESEM image of singe nickel dendritic microleaf where there are some particles aggregating at the bottom (see the part labeled by the dashed white block).
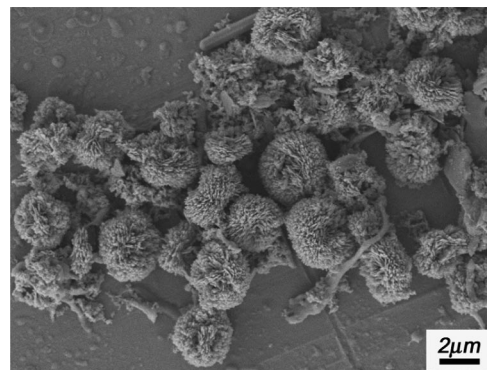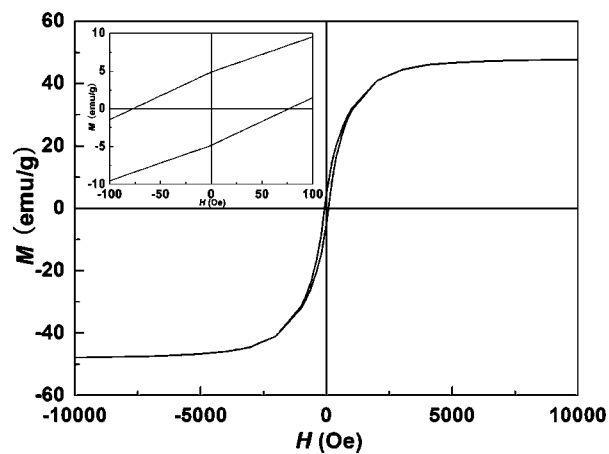
4. Conclusion

A distinctive type of nickel microleaf dendrite with length about 20 μm has been synthesized via a self-assembled solution route without any surfactant. Upon detailed studies, it is revealed that the stem first grows along [111], one unilateral branch grows along [$\bar{1}$11] and then the other unilateral branch grows along [100], respectively. The orientation of the stem is the magnetic easy axis of a cubic nickel crystal, which could possibly result in the decreased Hc for the sample. And the good crystallinity of the nickel dendritic microleaf would improve the Ms value. Additionally, formation of such dendritic structures requires two indispensable factors. One is a suitable low concentration of Ni(II) ions in the precursor solution. The other is that ferromagnetic nuclei induce Ni(II) ions to aggregate around the nickel nucleus and reduced to form the nickel storage. The present model could explain the formation of other dendritic ferromagnetic materials in equilibrium hydrothermal systems.

Supporting Information Available: XRD pattern. This material is available free of charge via the Internet at http://pubs.acs.org.

References

(1) Zhu, J.; Peng, H.; Chan, C. K.; Jarausch, K.; Zhang, X. F.; Cui, Y. *Nano Lett.* **2007**, *7*, 1905.
(2) Sukhanova, A.; Baranov, A. V.; Perova, T. S.; Cohen, J. H. M.; Nabiev, I. *Angew. Chem., Int. Ed.* **2006**, *45*, 2048.
(3) Yan, H.; He, R.; Johnson, J.; Law, M.; Saykally, R. J.; Yang, P. *J. Am. Chem. Soc.* **2003**, *125*, 4728.
(4) Tian, Z.G. R.; Liu, J.; Voigt, J. A.; Xu, H. F.; Mcdermott, M. J. *Nano Lett.* **2003**, *3*, 89.
(5) Parfenov, A.; Gryczynski, I.; Malicka, J.; Geddes, C. D.; Lakowicz, J. R. *J. Phys. Chem. B* **2003**, *107*, 8829.
(6) Zhu, J.; Liu, S.; Palchik, O.; Koltypin, Y.; Gedanken, A. *Langmuir* **2000**, *16*, 6396.
(7) Wang, M.; Liu, X. Y.; Strom, C. S.; Bennema, P.; Enckevort, W.; Ming, N. B. *Phys. Rev. Lett.* **1998**, *80*, 3089.
(8) Liu, X.; Li, R.; Wang, Y.; Qiu, G.; Zhang, N.; Li, X. *J. Phys. Chem. C* **2007**, *111*, 163.
(9) Fang, J.; You, H.; Kong, P.; Yi, Y.; Song, X.; Ding, B. *Cryst. Growth Des.* **2007**, *7*, 864.
(10) Cheng, F.; Zhao, J.; Song, W.; Li, C.; Ma, H.; Chen, J.; Shen, P. *Inorg. Chem.* **2006**, *45*, 2038.
(11) Chen, Z.; Shan, Z.; Cao, M. S.; Lu, L.; Mao, S. X. *Nanotechnology* **2004**, *15*, 365.
(12) Manna, L.; Milliron, D. J.; Meisel, A.; Scher, E. C.; Alivisatos, A. P. *Nat. Mater.* **2003**, *2*, 382.
(13) Witten, T. A.; Sander, L. M. *Phys. Rev. Lett.* **1981**, *47*, 1400.
(14) Fang, J. X.; You, H. J.; Kong, P.; Yi, Y.; Song, X. P.; Ding, B. J. *Cryst. Growth Des.* **2007**, *7*, 864.
(15) Meakin, P. *Phys. Rev. Lett.* **1983**, *51*, 1119.
(16) Kolb, M.; Botet, R.; Jullien, R. *Phys. Rev. Lett.* **1983**, *51*, 1123.
(17) Kuang, D.; Xu, A.; Fang, Y.; Liu, H.; Frommen, C.; Fenske, D. *Adv. Mater.* **2003**, *15*, 1747.
(18) Cao, M. H.; Liu, T. F.; Gao, S.; Sun, G. B.; Wu, X. L.; Hu, C. W.; Wang, Z. L. *Angew. Chem., Int. Ed.* **2005**, *44*, 4197.
(19) Zhao, Y.; Xie, Y.; Zhu, X.; Yan, S.; Wang, S. X. *Chem. Eur. J.* **2008**, *14*, 1601.
(20) Zitoun, D.; Respaud, M.; Fromen, M. C.; Casanove, M. J.; Lecante, P.; Amiens, C.; Chaudret, B. *Phys. Rev. Lett.* **2002**, *89*, 37203.
(21) Pileni, M. P. *J. Phys. Chem. B* **2001**, *105*, 3358.
(22) Shevchenko, E. V.; Talapin, D. V.; Schnablegger, H.; Kornowski, A.; Festin, O.; Svedlindh, P.; Haase, M.; Weller, H. *J. Am. Chem. Soc.* **2003**, *125*, 9090.
(23) Yang, L. X.; Zhu, Y. J.; Tong, H.; Wang, W. W.; Cheng, G. F. *J. Solid State Chem.* **2006**, *179*, 1225.
(24) Liu, Z. P.; Li, S.; Yang, Y.; Peng, S.; Hu, Z. K.; Qian, Y. T. *Adv. Mater.* **2003**, *15*, 1946.
(25) Xiong, Y.; Jing, Y.; Gu, X. Y.; Chen, Q. W. *J. Phys. Chem. C* **2007**, *111*, 6998.
(26) Zhu, L. P.; Xiao, H. M.; Zhang, W. D.; Yang, Y.; Fu, S. Y. *Cryst. Growth Des.* DOI: 10.1021/cg701036k.
(27) Zhu, Y. C.; Zheng, H.; Yang, Q.; Pan, A. L.; Yang, Z.; Qian, Y. T. *J. Cryst. Growth* **2004**, *260*, 427.
(28) Xu, R.; Xie, T.; Zhao, Y. G.; Li, Y. D. *Cryst. Growth Des.* **2007**, *7*, 1904.
(29) Han, M.; Liu, Q.; He, J. H.; Song, Y.; Xu, Z.; Zhu, J. M. *Adv. Mater.* **2007**, *19*, 1096.
(30) He, L.; Zheng, W. Z.; Zhou, W.; Du, H. L.; Chen, C. P.; Guo, L. *J. Phys.: Condens. Matter* **2007**, *19*, 036216.
(31) Zhang, H. T.; Wu, G.; Chen, X. H.; Qiu, X. G. *Mater. Res. Bull.* **2006**, *41*, 495.
(32) Mcintyre, N. S.; Cook, M. G. *Anal. Chem.* **1975**, *47*, 2208.
(33) Schreifels, J. A.; Maybury, P. C.; Swartz, W. E. *J. Catal.* **1980**, *65*, 195.
(34) Pashutski, A.; Hoffman, A.; Folkman, M. *Surf. Sci.* **1989**, *208*, L91.
(35) Martensson, N.; Malmquist, P. A.; Svensson, S.; Basilier, E.; Pireaux, J. J.; Gelius, U.; Siegbahn, K. *Nouv. J. Chim.* **1977**, *1*, 191.
(36) Kessler, D. A.; Koplik, J.; Levine, H. *Adv. Phys.* **1988**, *37*, 255.
(37) Ozturk, B.; Talukdar, I.; Flanders, B. N. *Nanotechnology* **2007**, *18*, 365302.
(38) Fujiwara, M.; Chie, K.; Sawai, J.; Shimizu, D.; Tanimoto, Y. *J. Phys. Chem. B* **2004**, *108*, 3531.
(39) Wan, D. F.; Ma, X. L. *Magnetic Physics*; Publishing House of Electronics Industry: Beijing, 1999; p 178.
(40) Liu, X.; Yi, R.; Wang, Y.; Qiu, G.; Zhang, N.; Li, X. *J. Phys. Chem. C* **2007**, *111*, 163.
(41) Wu, S. H.; Chen, D. H. *J. Colloid Interface Sci.* **2003**, *259*, 282.
(42) Hwang, J. H.; Dravid, V. P.; Teng, M. H.; Host, J. J.; Elliott, B. R.; Johnson, D. L.; Mason, T. O. *J. Mater. Res.* **1997**, *12*, 1076.
(43) Wu, M. Z.; Xiong, Y.; Jia, Y. S.; Niu, H. L.; Qi, H. P.; Ye, J.; Chen, Q. W. *Chem. Phys. Lett.* **2005**, *401*, 374.
(44) Liu, X. M.; Fu, S. Y. *J. Cryst. Grow.* **2007**, *306*, 428.
(45) Song, Q.; Zhang, Z. J. *J. Phys. Chem. B* **2006**, *110*, 11205.

CG800093M